Pergamon

Acta mater. 49 (2001) 3231–3242

Acta MATERIALIA

www.elsevier.com/locate/actamat

FRACTURE OF A TEXTURED ANISOTROPIC CERAMIC

M. H. ZIMMERMAN‡[1], D. M. BASKIN§[1], K. T. FABER[1]†, E. R. FULLER Jr.[2], A. J. ALLEN[2] and D. T. KEANE[1]

[1]Department of Materials Science and Engineering, Robert R. McCormick School of Engineering and Applied Scienc, Northwestern University, Evanston, IL 60208, USA and [2]National Institute of Standards and Technology, Gaithersburg, MD 20899, USA

(Received 29 March 2001; accepted 23 May 2001)

Abstract—The role of crystallographic texture in determining the fracture behavior of a highly anisotropic ceramic, iron titanate, has been examined. By exploiting the anisotropy in its single crystal magnetic susceptibility, crystallographically textured and untextured iron titanate microstructures were formed by gelcasting in the presence and absence of a strong magnetic field, respectively. The magnetic field-assisted processing imparted a fiber-like texture to the processed ceramic material in which the crystallographic *b*-axes of the grains aligned parallel to the applied field. Triaxial residual stress and lattice parameter measurements showed that both the untextured and textured materials had undergone significant stress–relaxation, presumably due to spontaneous microcracking. Further, 'aggregates' of non-textured material were discovered within textured material that led to a population of meso-scale cracks (meso-cracks) in the microstructure oriented normal to the direction of alignment. Both crack populations were examined using a finite element simulation and confirmed by small angle neutron scattering measurements, and for meso-cracks, by X-ray tomography. Bend strength and R-curve behavior were evaluated as a function of texture and orientation in the magnetically processed materials. Strengths remained within 20% of that of the control material, except for one orientation, for which the strength decreased with increasing degree of texture due to favorably oriented meso-cracks. The R-curve behavior was highly anisotropic, with the peak fracture toughness of the magnetically processed material ranging from approximately equal to 2.5 times that of the control material. Additionally, the peak fracture toughness of each orientation increased with the degree of texture. Anisotropic fracture properties were related to interactions between the test crack and the population of meso-cracks.

Keywords: Ceramics; Fracture & fracture toughness; Small angle neutron scattering; Texture

1. INTRODUCTION

One of the primary causes of anisotropy in the properties of polycrystalline materials is texture. Texture, or the presence of a nonuniform distribution of grain orientations, imposes single crystal anisotropies onto the properties of the bulk material. The degree of the bulk property anisotropies depends on the strength and type of texture, as well as the degree of anisotropy in the single crystal properties. The studies described here assess the role of texture on the fracture behavior of a highly anisotropic ceramic with a known propensity for microcracking. Iron titanate, Fe_2TiO_5, was studied because it exhibits strong anisotropy in both its thermal expansion and magnetic susceptibility [1–3], as shown in Table 1. As a result of its thermal expansion anisotropy, Fe_2TiO_5 is prone to microcracking, even at relatively small grain sizes [4]. Spontaneous microcracking, its grain size dependence and influence on mechanical behavior has been studied in a variety of ceramics [5–15]. Control of microcracking by texturing has been given significantly less attention [16], and is, therefore, the focus of the current work.

Because of its anisotropic magnetic susceptibility, texture may be imposed on the microstructures of

Table 1. Coefficients of thermal expansion and magnetic susceptibility of Fe_2TiO_5

Axial direction	Coefficient of thermal expansion ($°C^{-1}$)	Susceptibility ($\times 10^{-8}$ m^3/mol)
a	10.1×10^{-6}	4.22
b	16.3×10^{-6}	5.16
c	0.6×10^{-6}	3.78

† To whom all correspondence should be addressed. Tel.: +1-847-491-3537; fax: +1-847-491-7820.

E-mail address: k-faber@northwestern.edu (K. T. Faber)

‡ Current address: GE Suprabarasives, Worthington, OH, USA.

§ Current address: DaimlerChrysler AG, Ulm, Germany.

PII: S1359-6454(01)00224-5

polycrystalline Fe_2TiO_5 via magnetic field-assisted processing. Imperative to understanding the role of texture in these materials is the ability to produce by the same processing route both crystallographically textured and untextured microstructures for comparison. Gelcasting, when used in conjunction with magnetic field-assisted processing, fulfills this need. Characterization of the imposed texture via X-ray pole figures provides information about the orientation distribution of grains in the polycrystals. The fracture behavior of the textured materials is evaluated and compared to that of the untextured material. Both fracture strength and crack growth resistance are measured in three directions relative to the texture symmetry. Since changes in crystallographic texture are likely to be accompanied by changes in microcracking behavior, the crack population is evaluated via small angle neutron scattering, and in the case of mechanical test specimens, X-ray tomography. Finally, an object-oriented finite element analysis is used for residual stress simulations to compare expected with observed mechanical behavior.

2. EXPERIMENTAL DETAILS

2.1. Processing

Fe_2TiO_5 samples for this study were made using gelcasting. The intrinsic idle time associated with the polymerization step makes gelcasting particularly well suited for magnetic field-assisted processing. During the idle time associated with gelcasting, a suspension may be placed in an applied magnetic field. Prior to the onset of polymerization, a particle is free to rotate under the influence of the magnetic field, thus aligning itself such that its direction of maximum susceptibility is parallel to the field direction. Once the polymerization process is complete, the gel network locks the particle in place, and the assembly can be removed from the magnetic field without disturbing the imposed orientation.

The acrylamide system [17] was used for gelcasting. This system consisted of a premix of acrylamide (AM) monomers and a cross-linking agent, methylenebisacrylamide (MBAM) monomers; a catalyst, ammonium persulfate (APS); and an activator, tetramethylethylenediamine (TEMED). A dispersant and an anti-foaming agent are added to the acrylamide premix immediately prior to adding the powder. Iron titanate powder is added to the premix of AM and MBAM forming a suspension with 30 vol% solids content. A lower solids loading than typical for gelcasting was chosen to reduce particle–particle interaction, allowing easy particle rotation. The suspension was then placed in an ice water bath and cooled to 2–3°C to extend the idle time between the addition of the catalyst and the onset of polymerization. After 30 min, APS solution and TEMED were mixed into the suspension. Further details of the process can be found in reference [18].

The suspension was cast into a Delrin† mold, degassed in a vacuum dessicator, and lowered into the bore of a magnet, where it remained for 3 h. Processing was carried out at two field strengths, 3.2 and 8.4 T. Two mold configurations designated as Type 1 and Type 3 [shown in Fig. 1(a)] allowed processing of samples having different texture orientations with respect to the sample coordinate system. Control samples were processed in the same manner, outside of the magnetic field.

After mold removal the samples were dried 24 h in air. The dry green bodies were then placed in a vented furnace for burnout of the gel binder at 575°C for 6 h. The resulting powder compacts were isostatically pressed at 276 MPa to increase the green density without disturbing the particle orientations [19]. Specimens were sintered for 1 h at 1170°C in air.

2.2. Microstructural evaluation

2.2.1. Optical microscopy. Grain sizes were measured on polished surfaces using the mean intercept technique [20]. Additionally, grain size was measured as a function of orientation. Surfaces were also examined and rotated in polarized light to qualitatively evaluate crystallographic texture. A non-textured specimen will reflect polarized light at the same intensity regardless of orientation, while textured

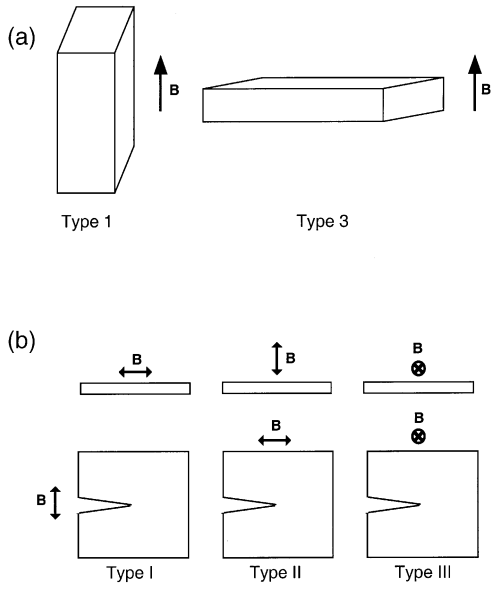

Fig. 1. (a) Schematic of the Type 1 and Type 3 configurations used in magnetic field (**B**) assisted processing. (b) Schematics of three types of textured samples for strength (upper) and R-curve (lower) measurements.

† Information on commercial products is given for completeness and does not necessarily constitute or imply their endorsement by the National Institute of Standards and Technology.

specimens will vary from light to dark during rotation [21].

2.2.2. Small angle neutron scattering. Small angle neutron scattering (SANS) provides a means of characterizing microstructural features, such as precipitates, pores or cracks which range in size from 1 nm to 1 μm [22, 23] making it an ideal method for characterizing the microcrack population in Fe_2TiO_5. At sufficiently large scattering vectors Q, the scattered intensity, I, from the scattering phase (cracks in this case) may be described by the Porod approximation [24]:

$$I \approx \frac{d\Sigma}{d\Omega} = 2\pi(\Delta\rho)^2 \frac{S_V}{Q^4}$$

where $d\Sigma/d\Omega$ is the macroscopic scattering cross-section, $\Delta\rho$ is the difference in scattering length density between phases on each side of the scattering interface, i.e., between the Fe_2TiO_5 and the crack, so that it is the scattering length of Fe_2TiO_5, and S_V is the surface area per unit sample volume of the scattering phase. SANS experiments were performed on the control sample and Types 1 and 3 processed under 3.2 and 8.4 T at the National Institute of Standards and Technology (NIST) using an 8 m SANS instrument [25]. Studies were performed using a 0.6 nm wavelength across two different scattering vector (Q) ranges. For control samples and those processed at 3.2 T, the Q range was from 0.06 to 2.0 nm^{-1}. For samples processed at 8.4 T, the Q range was from 0.15 to 1.0 nm^{-1}. Typically, only the data for $Q > 0.1$ nm^{-1} were used in the Porod analyses.

For each specimen, the SANS data were corrected for variations in the detector sensitivity, attenuation within the specimen, and background scattering. Additionally, the data were calibrated against a standard scatterer. The reduced data were radially averaged about the beam center to obtain the absolute scattering cross-section $d\Sigma/d\Omega$ versus Q. The data were also sector-averaged about the beam center to examine the dependence of any anisotropic scattering on the azimuthal angle ϕ.

2.2.3. X-ray tomography. X-ray tomography (XTM) was used to image through-the-thickness sections of mechanical test specimens from tests which were halted prior to catastrophic failure. XTM studies were performed on textured Fe_2TiO_5 at beamline X2B at the National Synchrotron Light Source at Brookhaven National Laboratory [26, 27]. Right parallelepiped specimens of textured Fe_2TiO_5 with nominal dimensions of 0.8×0.8×4 mm were mounted to a goniostat placed atop a rotation stage. XTM specimens were sectioned from used mechanical testing specimens that contained intact crack tips. XTM specimens were oriented such that the crack front was parallel to the long axis of the XTM specimen. The direction of magnetic alignment within the specimen was in the crack plane and perpendicular to the long axis of the specimen. The white X-ray beam from the synchrotron was monochromated by a single bounce Si(111) monochromator, choosing a wavelength of 0.48 Å. The X-ray beam transmitted through the sample was incident on a phosphor screen, which was imaged at 20× resolution onto a CCD chip with 27 μm^2 pixels, giving an effective resolution in the X-ray radiographs of 1.35 μm^2 pixels. Images of the sample were taken through a 180° rotation in 0.12° increments, collecting for 5 s at each point. The images were processed with an Exxon developed reconstruction algorithm to give the three-dimensional absorption map of the entire sample volume.

2.3. Residual stresses and texture

2.3.1. Residual stress simulations. Two-dimensional finite element simulations were performed using the program OOF, an object oriented finite element analysis developed at the Center for Computational and Theoretical Materials Science at NIST [28]. The program OOF is a combination of two programs. The first program, PPM2OOF, is designed to read an image file such as a micrograph. The individual pixels that constitute the micrograph may be collected into groups and their material properties assigned. For instance, the elements corresponding to a specific grain or collection of grains may be grouped together as a single unit. Material properties that may be assigned to the groups include Young's modulus, Poisson's ratio, the single crystal thermal expansion coefficients, and the crystallographic orientation through Euler angles. Although anisotropic elasticity is possible, isotropic elasticity was assumed for the current simulation. Once the material properties are assigned, PPM2OOF creates a file containing the finite elements, which the second program, OOF, then reads.

OOF performs the finite element calculations on the files created by PPM2OOF. Boundary conditions, changes in temperature and distortions to the finite element mesh may all be applied using the OOF interface. Once a change has been introduced, OOF equilibrates the microstructure and determines the stress state in every element in the mesh.

At the microstructural scale, regions of non-textured islands within a textured Fe_2TiO_5 matrix were examined using this method. A rectangular mesh of elements was constructed and random circular clusters of several elements throughout the mesh were selected. The textured matrix was assigned the properties of textured Fe_2TiO_5 with Euler angles consistent with alignment in the 'l' direction. For a 'perfectly' textured sample, this gives a coefficient of thermal expansion (CTE) in the x-direction equal to that of the b-axis (16.3×10^{-6}/°C) of Fe_2TiO_5 while the y-direction is assigned a CTE equal to an average of the CTE's of the a- and c-axes (5.35×10^{-6} /°C). The non-textured aggregate is assigned a CTE equal to an average of all the axes, or 9.0×10^{-6}/°C. These

elements were assigned thermal and elastic properties consistent with non-textured Fe_2TiO_5. The microstructure was cooled 1000 K and allowed to re-equilibrate via the finite element calculations, assuming plane stress conditions.

2.3.2. Residual stress and texture measurements. Pole figures were measured on polished surfaces of both control and magnetically processed specimens. Orientation distribution functions (ODFs) were determined from these experimentally measured pole figures using the WIMV algorithm [29–31]. Texture was assessed by examining the axial pole figures calculated from these ODFs. Details of these studies were reported in previous papers [32], and the results are summarized in Table 2. Samples processed in the 3.2 T field are designated weakly textured, while those processed in the 8.4 T field are designated strongly textured.

Triaxial residual stress measurements were made using X-ray diffraction. The (262) peak, located at approximately 144.3° 2θ, was chosen to provide a high degree of accuracy. For a given stress measurement, 31 $\phi\psi$ combinations were examined. The angle ϕ was varied from 0° to 300° in 60° steps. At each angle ϕ, 2θ scans were recorded at ψ angles corresponding to $\sin^2\psi = 0.1$, 0.2, 0.3, 0.4 and 0.5. Additionally, at $\phi = 0°$, the 2θ value corresponding to $\sin^2\psi = 0$ was measured. All ψ tilts were performed in ψ-goniometry in which the ψ axis is coincident with the θ axis. Data were collected from 143.6° to 145.5° 2θ in 0.05° steps with a 60-s dwell time. For cases where the texture resulted in low peak intensities, the dwell time was raised to 120 s. For triaxial residual stress measurements, values for the strain-free lattice spacings are necessary. These were determined by measuring the 2θ locations of several peaks in annealed powder sample of Fe_2TiO_5 mixed with a Si powder standard. Peaks were fit to a Gaussian function using a software program, Peakfit [33] to account for background and deconvolute the $K\alpha_1$ and $K\alpha_2$ peaks. Residual strains and stresses were determined using a least-squares method [34] and a computer software program, TRIAX [35].

Table 2. Texture strength and residual stress matrices of non-textured and textured Fe_2TiO_5

Sample	Texture Strength in MRD	$\sigma_{ij} = \begin{vmatrix}\sigma_{11} & \sigma_{12} & \sigma_{13}\\ \sigma_{21} & \sigma_{22} & \sigma_{23}\\ \sigma_{31} & \sigma_{32} & \sigma_{33}\end{vmatrix}$ in MPa		
Control, 0 T	0.9–1.4	−13.5±2.5	1.2±1.2	−1.2±0.4
		1.2±1.2	−15.1±2.6	−0.4±0.4
		−1.2±0.4	−0.4±0.4	−2.9±1.2
Type 1, 3.2 T	3 {0k0}	−19.3±3.7	0.5±1.1	0.5±0.5
		0.5±1.1	−18.7±2.6	0.4±0.4
		0.5±0.5	0.4±0.4	−3.3±1.5
Type 3, 3.2 T		−8.7±2.2	0.6±1.1	0.4±0.4
		0.6±1.1	−13.4±2.3	−0.2±0.4
		0.4±0.4	−0.2±0.4	−2.9±1.1
Type 1, 8.4 T	48 {0k0}	−7.9±4.8	0.8±1.2	0.2±0.7
		0.8±1.2	−20.0±3.0	−0.7±0.5
		0.2±0.7	−0.7±0.5	0.8±1.9
Type 3, 8.4 T		−30.7±2.0	0.8±0.7	0.2±0.3
		0.8±0.7	−27.5±2.0	0.2±0.3
		0.2±0.3	0.2±0.3	−1.9±1.3

2.4. Mechanical testing

Four-point flexure and short double cantilever beam (sDCB) tests were used to characterize the strength and crack growth resistance (R-curve) behavior of the iron titanate samples, respectively. To examine these properties as a function of direction, three different *b*-textured samples were tested with respect to orientation [Fig. 1(b)]. The Type I and Type II specimens were machined from Type 1 samples, described in Section 2.1, while the Type III specimens were machined from Type 3 samples. A Type I specimen corresponds to the orientation in which the applied field is perpendicular to both the crack plane and the direction of crack propagation. A Type II specimen corresponds to the orientation in which the applied field is parallel to both the crack plane and the direction of propagation. Finally, a Type III specimen corresponds to the orientation in which the applied field is parallel to the crack plane, but perpendicular to the direction of propagation.

Strength measurements were made in accordance with test methods described in ASTM C1161-94 [36] Specimens with dimensions 1.5×2.0×>25 mm were loaded on 20 mm outer and 10 mm inner spans having 2.0 mm nominal bearing diameters. At least 30 samples were tested for each sample type.

Short double cantilever beam specimens with nominal dimensions 30×25×2.5 mm were machined from gelcast samples. For in situ crack length measurements, the specimens were then polished to 0.3 μm finish. Holes for pin loading the specimens were ultrasonically drilled in the specimens. The specimens were then notched with a diamond wafering blade to a notch length $a_0 = 18$ mm. A sharp crack was introduced at the notch tip by wedge loading, typically yielding an initial crack length beyond the notch length.

The pre-cracked sDCB specimens were pin loaded on a servo-electric testing machine. Tests were conducted at a constant crosshead displacement of 5.0 μm/min, during which load, crosshead displacement and crack mouth opening displacement were recorded at a sampling rate of 1 Hz using a data acquisition system. Crack mouth opening displacement was monitored using an extensometer via two knife-edges mounted in grooves machined into the specimen end. Crack mouth opening displacement was converted to crack opening displacement, and stress intensity factor, K, were calculated from the method of Kanninen [37]. Crack length was monitored during the course of the test using a traveling microscope attached to a digital micrometer. Prior to failure, specimens were unloaded to allow the crack paths to be examined via optical microscopy. Three samples were tested for each sample type.

3. RESULTS AND DISCUSSION

3.1. Microstructural observations

A representative optical micrograph of a gelcast and sintered sample is shown in Fig. 2(a). Of note is an equiaxed grain morphology despite the crystallographic texture. Rose patterns indicated that the grain size remained invariant with direction and with field strength in all samples, averaging approximately 5.8 μm. Additionally, grain sizes measured on the cross-sections of the control samples were similar to those on the surfaces.

Inspection of textured materials revealed several unusual microstructural features related to processing and texture. The most conspicuous can be seen on machined or fractured surfaces with the naked eye. They appear as small (up to 1.5 mm in diameter) 'aggregates' that are slightly lighter in color than the surrounding material [Fig. 2(b)]. By rotating the textured material during observation using a polarized light microscope, it was found that 'aggregates' maintain constant brightness whereas the matrix in between aggregates flashes from light to dark as the perch is rotated, suggesting non-textured islands in a matrix of textured Fe_2TiO_5.

In order to quantify this effect, a photoresistor circuit was connected to the microscope's eyepiece [38]. The photoresistor caused the current to scale with the intensity of light it received—the brighter was the image, the higher the current was. Output currents from the circuit were recorded as the sample was rotated. Initially the microscope was focused exclusively on an area between aggregates, and then refocused exclusively on an aggregate. The results for both cases are presented in Fig. 3 which clearly shows a sinusoidal output for data collected between the aggregates. Although the aggregate produced a sinusoidal wave as well, the peaks are roughly an order of magnitude smaller in amplitude. This behavior implies that the aggregates, while textured, are quite poorly aligned compared to their surroundings. As a further check, a control sample was examined using the same method and produced constant brightness during rotation.

One possible explanation for lack of texture in the aggregates is that they correspond to the gel reaction centers where crosslinking initiates [39]. Because these sites gel most quickly, Fe_2TiO_5 particles in the very near vicinity will have little opportunity to align. In contrast, particles farther away from reaction centers have a much larger opportunity to align. This hypothesis provides a basis to explain a microstructure with local variations in texture. Admittedly, it may not explain why the gradient between aggregates and matrix is not more gradual.

A phenomenon known as depletion flocculation may provide an alternate explanation [40]. Consider many particles separated by distances too small to accommodate a polymer chain. The chemical potential for water in between the particles is larger than that outside of the gap. Equilibrium will dictate that the chemical potential for water in the gap be reduced. Thus, the system will act to reduce the concentration of water in the gap. Accordingly, the particles will flocculate. Flocculation will reduce the mobility of the particles which in turn reduces the opportunity for alignment. This hypothesis may

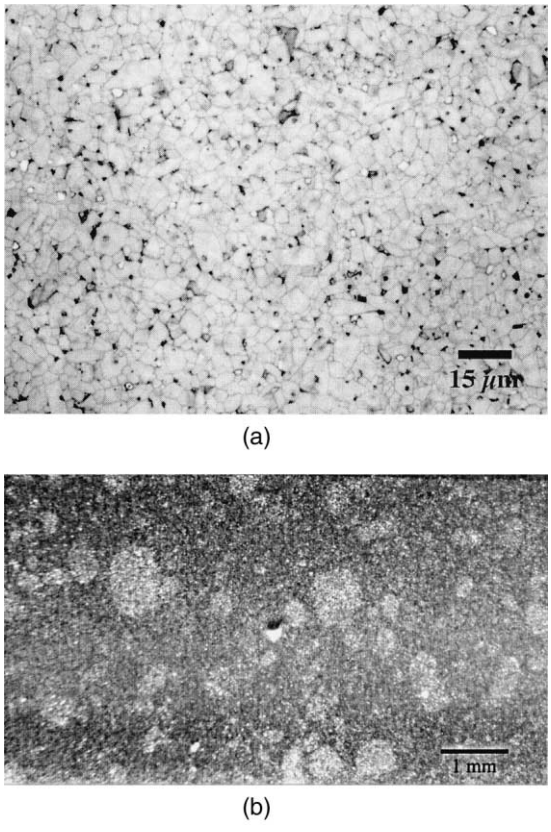

Fig. 2. Optical micrographs of gelcast samples processed in an 8.4 T magnetic field: (a) a high magnification image illustrating the typical microstructure and (b) a low magnification image showing 'aggregate' formation.

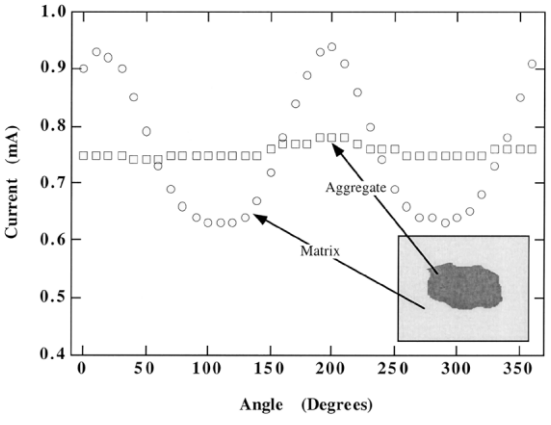

Fig. 3. Results from the cross-polarization experiment of a photoresistor circuit as a function of rotation angle for the 'aggregate' and surrounding matrix.

account for the sharp gradient in texture between aggregates and matrix, although the dispersant (Darvan C) used in this study should have prevented depletion flocculation by controlling inter-particle distances from becoming sufficiently small.

In the case of specimens processed at 8.4 T, large differences in the degree of texture between the non-textured islands and the matrix lead to thermal-mismatch derived cracks. These meso-scale cracks or meso-cracks, 50–300 μm in length, originate at the non-textured island boundaries and grow perpendicular to the direction of alignment. Residual stress arising from the islands of non-textured material provides a consistent explanation for the prevailing crack position. SANS results and finite element modeling described later will substantiate this claim.

In addition to a population of meso-cracks, the material also is believed to have a population of microcracks. The critical grain size for spontaneous microcracking in randomly oriented Fe_2TiO_5 is found to be in the range of 3 μm. Given that the average grain size in this study is over 5 μm, spontaneous microcracks are believed to occur in this material, though not visible using optical microscopy.

3.2. SANS

The scattering data for the control and textured specimens processed in a 3.2 T field were averaged in 30° sectors at 15° intervals about the beam center. Plots of the apparent Porod constant ($Q^4\,d\Sigma/d\Omega$) versus the azimuthal angle ϕ are given in Fig. 4. It should be noted that the direction of maximum Porod scattering corresponds to the preferred direction of the small dimension of the scattering species, in this case cracks. The small dimension corresponds to the normal to the crack plane. Both the control and Type 3 specimens exhibited circularly symmetric Porod scattering [Fig. 4(a) and (c), respectively]. The Type 1 specimens, however, displayed a notable degree of anisotropy, shown in Fig. 4(b), with a maximum apparent Porod constant oriented parallel to the magnetic field direction, i.e. the normal to the crack plane. This indicates that the meso-cracks in the weakly textured microstructure exhibited a moderate degree of preferred orientation perpendicular to the applied field.

The scattering data for the textured specimens processed in an 8.4 T field were averaged in 20° sectors at 10° intervals about the beam center, rather than the 30° sectors used on the aforementioned data. Like the Type 3 specimen processed in the 3.2 T applied field, the Type 3 specimen processed in the 8.4 T applied field exhibited a circularly symmetric apparent Porod constant, and is not shown. However, the Type 1 exhibited highly anisotropic Porod scattering, as evidence in Fig. 5(a). Two orthogonal anisotropic components are readily apparent. The larger component is in the direction that coincides with the applied magnetic field and is consistent with the pre-existent meso-cracks which were oriented so that their planes

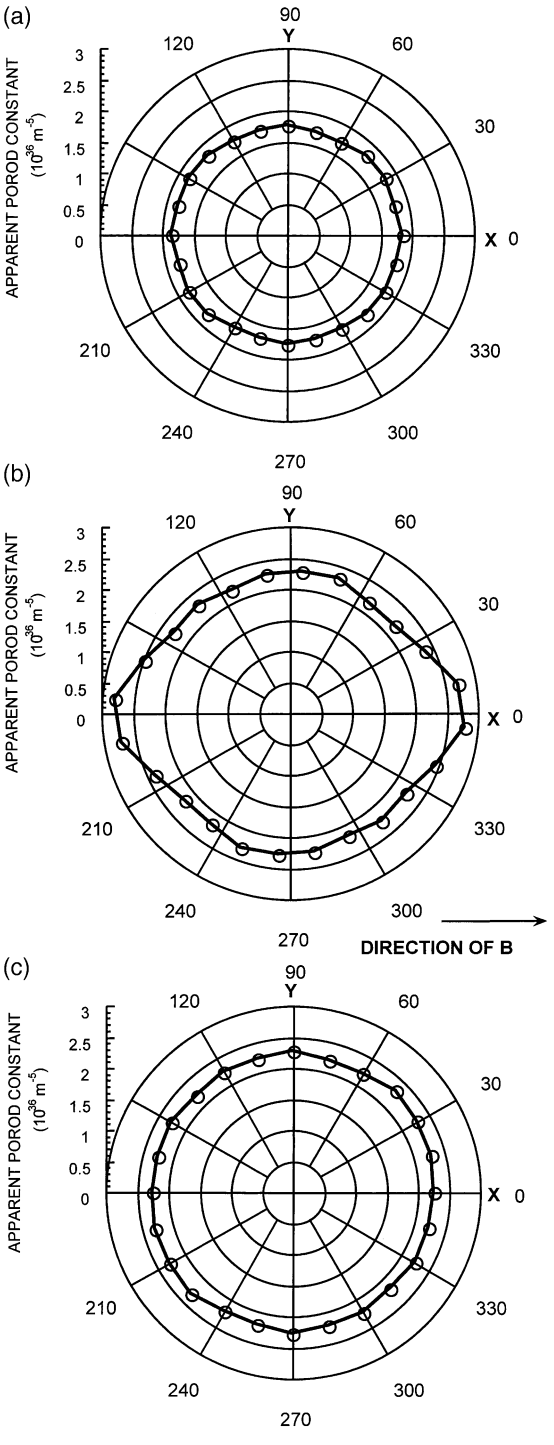

Fig. 4. Apparent Porod constant versus azimuthal angle for (a) control sample (b) Type 1 specimen processed in a 3.2 T magnetic field and (c) Type 3 specimen processed in a 3.2 T magnetic field. In (c) the applied magnetic field is normal to the page.

were perpendicular to the field direction. The second component, which was not observed in the previous specimens, lies in a direction perpendicular to the applied magnetic field and is consistent with the microcracking predicted by the texture and thermal

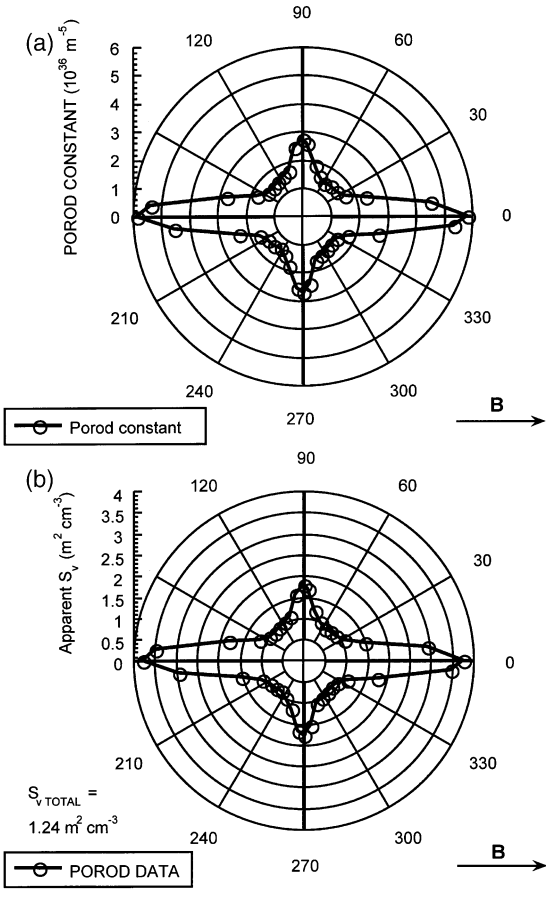

Fig. 5. (a) Apparent Porod constant and (b) apparent surface area, S_V^{app} versus azimuthal angle for a Type 1 specimen processed in an 8.4 T applied magnetic field. Note that the magnetic field is horizontal to the plane of the page.

expansion anisotropy. Such microcracks would be oriented so that their planes are parallel to the applied field direction and are uniformly distributed in the plane perpendicular to the field. This is consistent with the isotropy in the scattering observed in all the Type 3 specimens combined with the anisotropy observed in Type 1 specimens.

In Fig. 5(b) the apparent surface area per unit volume S_V^{app} was calculated from the Porod constants determined from Fig. 5(a) to illustrate the anisotropy in the scattering population. For these calculations, a neutron scattering length density $|\Delta\rho| = 4.956\times10^{14}$ m^{-2} is used. Modeling of the apparent surface areas presented in Fig. 5(b) has established that the crack population can be described using a combination of spherical pores and oblate spheroidal elements [41]. The oblate spheroidal elements are further broken into a population whose short dimension is aligned parallel to the magnetic field direction and a population whose short dimension is perpendicular to the field. The first population is consistent with the predictions of likely microcrack sites. The second population is consistent with observed meso-cracks aligned perpendicular to the magnetic field direction in the specimens processed in the 8.4 T applied field, both of which are predicted by the finite element modeling.

After 3D orientational averaging of the anisotropic surface area distribution, the total surface area, S_V^{TOTAL} of the Type 1 specimen was determined to be 1.24±0.04 m^2 cm^{-3}. The standard deviation is the uncertainty determined from the computed straight-line fit to $\{Q^4I(Q)\}$ versus Q^4. This surface area marks a slight reduction with respect to that of the control sample, where $S_V^{TOTAL} = 1.37\pm0.02$ m^2 cm^{-3}. From these results, it appears that texturing may play a role in reducing the microcrack population which occurs spontaneously on cooling from thermal expansion anisotropy.

It should also be noted that the scattering information presented comes from populations of both pores and cracks. Since the pore morphology is spherical, it may be treated as isotropic with regard to scattering. As a result, the variations of scattering intensity with orientation may be attributed to preferred orientation of cracks in the microstructure.

3.3. Residual stresses

3.3.1. Residual stress simulations. OOF results for the non-textured islands in a textured matrix are shown in Fig. 6(a). The results clearly show tensile stress concentrations on the poles of the simulated non-textured islands oriented such that the field direction is perpendicular to the poles, and compressive stresses concentrating at the equator. Residual stress arising from the islands of non-textured material provides a consistent explanation for the prevailing crack position, as pictured in the schematic of Fig. 6(b). The textured matrix is assigned a coefficient of thermal expansion of 16.3×10^{-6}°C^{-1} (equal to that of the $b-$axis) in the direction parallel to the field direction and 5.35×10^{-6}°C^{-1} (equal to the average of the *a*- and *c*-axes) perpendicular to the field direction. The non-textured islands were assigned a CTE equal to the average of each of the axes, or 9.0×10^{-6}°C^{-1}. Given these values, as the material is cooled, a tangential tensile stress, perpendicular to the field direction and shown schematically in Fig. 6(c), develops in the matrix at the poles from the thermal mismatch. A smaller radial tensile stress also develops at the poles. The stress state is reversed at the equator: radial compression with a smaller tangential compression. For a textured sample, local microcracking can result for the remnant thermal expansion anisotropy in the *a*- and *c*-axes, and from the radial tensile stresses at the poles of the non-textured islands. However, these cracks soon propagate into compressive regions and arrest. In contrast, the tangential tensile stresses at the poles tend to overlap with those from the neighboring islands, as shown with the dashed lines in Fig. 6(a), and this is consistent with the development of meso-cracks perpendicular to the alignment direction. Furthermore, as the degree of

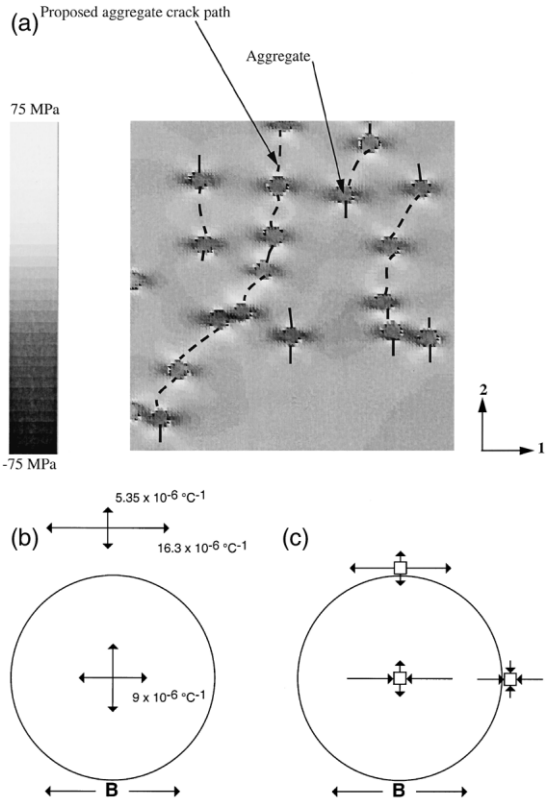

Fig. 6. (a) Simulation of σ_{11} for a textured matrix containing islands of non-textured materials (aggregates). Note high tensile stresses at the poles of the aggregates. The 'one' direction is parallel to the alignment direction. Schematic of non-textured aggregate in a textured matrix demonstrating (b) CTEs and (c) residual stress directions.

texture decreases, these stresses decrease in magnitude.

3.3.2. Residual stress measurements. The calculated stress matrices from the triaxial stress measurements are provided in Table 2. Note that the 33 direction corresponds to the specimen surface normal results. Typical goodness-of-fit parameters [35] for these measurements were greater than 0.5. Note that the '22' direction for the Type 1 specimens corresponds to the direction of applied magnetic field. The triaxial measurements show the presence of virtually no appreciable residual stresses. This is true for the control and the textured materials, regardless of texture strength. It should be noted that slightly compressive stresses are evident in all the materials. These may be due to volume expansion associated with the formation of cracks, which may provide some compression in the near surface layer.

Again, these measurements suggest significant stress relaxation has occurred. A likely source of this relaxation, even in the case of the textured materials, is through the formation of meso-cracks noted earlier, as well as spontaneous microcracks. Despite the presence of strong crystallographic texture in the magnetically processed materials, spontaneous microcracking is still quite likely to have occurred during processing. Consider the texture imposed through magnetic processing, in which the *b*-axes align preferentially in the direction of the applied field, while the *a*- and *c*-axes are uniformly distributed in the plane perpendicular to the field. Even if the texture was perfect, a significant anisotropy still exists in the plane perpendicular to the field. In this case, the anisotropy occurs between the *a*- and *c*-axes (see Table 1). In the absence of any texture the maximum thermal anisotropy occurs between the *b*- and *c*-axes. Essentially, the imposition of crystallographic texture has confined the thermal mismatch strains to one plane, but has not removed them.

One possible product of the confinement of these mismatch strains is the evolution of local residual stresses which themselves are greatest within the same plane. As a result, those grain boundaries whose normals lie in the plane perpendicular to the *b*-axis would develop the highest tensile residual stresses and would be the most likely to microcrack. The net result would be two-fold. First, the residual stresses would still be relieved by spontaneous microcracking. Second, the spontaneous microcracks would exhibit preferred orientation such that their normals would be uniformly distributed within the plane perpendicular to the *b*-axis. Both these hypotheses are consistent with the SANS observations reported in Section 3.2.

3.4. Mechanical tests

Flexural strengths as a function of specimen type and peak texture strength are shown in Fig. 7. Within the group of weakly textured specimens, notable strength anisotropy was evident, with the bend strength nearly doubling from the Type I to Type II specimens and further increasing in the Type III. In the strongly textured specimens, anisotropy in the fracture strength is still evident, with the Type I specimens exhibiting strength roughly half of that of Types II and III. However, the strengths of the latter two specimen types were nearly identical. Variations relative to the control specimens were insignificant for the Types II and III specimens, with the exception of the weakly textured Type III, whose strength was the

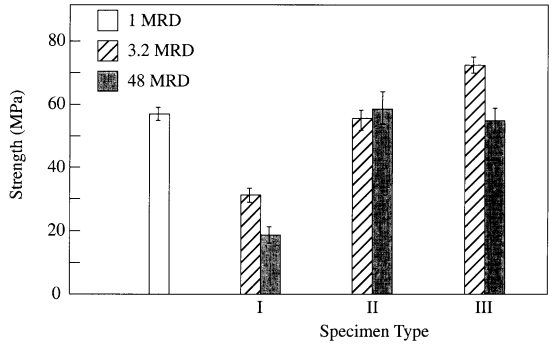

Fig. 7. Strength in bending as a function of specimen type and peak texture strength.

higher. Only the Type I specimens showed a large variation in strength relative to the control material.

The primary source of the anisotropy in the strongly textured specimens appears to be the presence of the parallel meso-cracks described earlier. In the Type I geometry, these parallel cracks were oriented perpendicular to the longest dimension of the bend bars and were likely to serve as the critical flaws from which failure initiated. In the other geometries, these meso-cracks were parallel to the to the longest dimension of the bend bars, making them unlikely failure initiation sites. However, the secondary crack system identified by SANS in Fig. 5 (where the crack plane contains the texture axis) can provide some fraction of cracks to be favorably oriented to reduce the strength.

3.4.1. Crack growth resistance behavior. The results of the sDCB tests for representative samples from each specimen type are given in Fig. 8. The R-curves of control and Types I, II, and III samples processed in the 8.4 T field are presented. The cracks are grown to lengths of up to 2.5 mm. Two representative samples are shown to demonstrate the reproducibility of the tests. The crack growth resistance curves for the control sample [Fig. 8(a)] were nearly flat, starting from an initial toughness that may be extrapolated to approximately 1 MPa.m$^{1/2}$, and reaching a peak value of approximately 1.6±0.08 MPa.m$^{1/2}$, where ± values represent one standard deviation of the mean. The lack of significant toughening is consistent with a fine-grained ceramic material which has also undergone spontaneous microcracking.

The results for the highly textured microstructures are presented in Fig. 8(b)–(d). Figure 8(b) corresponds to Type I specimens, while Fig. 8(c) and (d) correspond to Type II and Type III specimens, respectively. The fracture behavior of the highly textured specimens was very anisotropic, with the Type II specimens showing the highest peak toughness at approximately 4.0±0.2 MPa.m$^{1/2}$, followed by the Type III at approximately 3.0±0.16 MPa.m$^{1/2}$, and the Type I at 1.9±0.08 MPa.m$^{1/2}$. The highly textured Type II and Type III specimens exhibited higher peak toughness than the corresponding weakly textured specimens in all of the three orientations, as is summarized in Fig. 9.

The consistently higher toughnesses in the Type II and Type III highly textured specimens relative to the weakly textured specimens may be explained by two

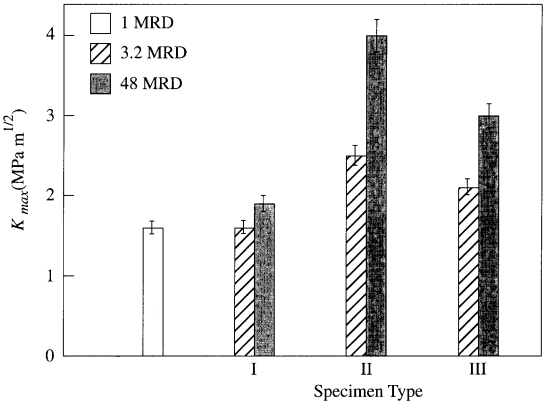

Fig. 9. Peak toughness as a function of specimen type and peak texture strength.

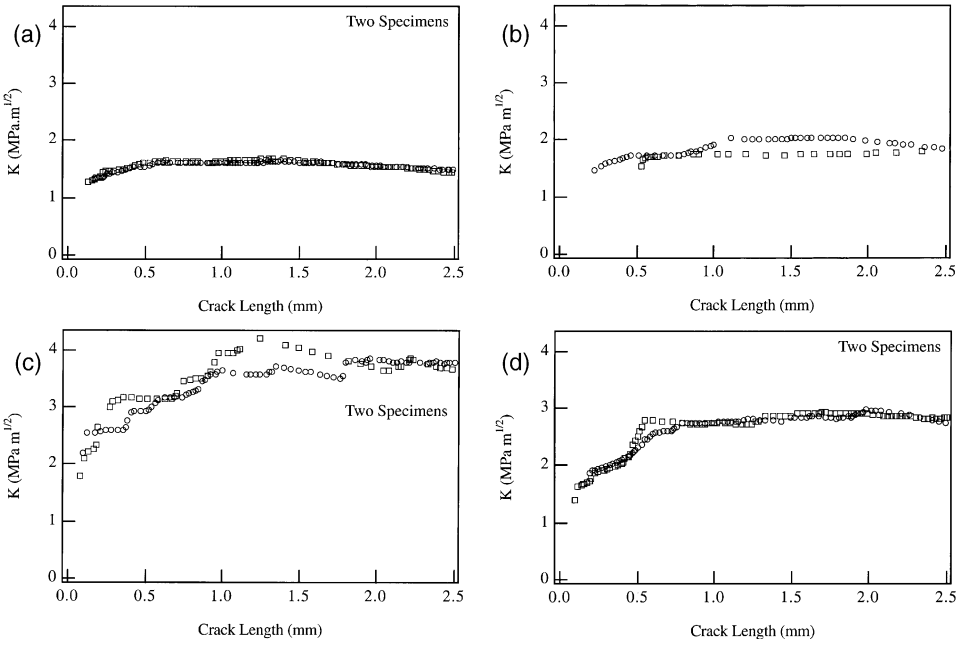

Fig. 8. Typical crack growth resistance behavior of (a) control material (b) Type I specimen processed in an 8.4 T magnetic field (c) Type II specimen processed in a 8.4 T magnetic field, and (d) Type III specimen processed in a 8.4 T magnetic field.

factors. First, toughness is directly proportional to Young's modulus [42]. The highly textured specimens had higher Young's moduli than the corresponding weakly textured specimens. The Young's modulus of the highly textured sample was anisotropic. However, the magnitude of that anisotropy is not sufficient to account for more than a small fraction of the anisotropy in fracture behavior; the modulus only varied by a maximum of 10%, while the fracture toughness varied by a factor of two. The second, overriding factor in the highly textured materials is the presence of the parallel meso-cracks in the microstructure. These cracks may serve as natural crack deflection sites for the test crack, as seen in Fig. 10(b). The test crack was often deflected for hundreds of microns along the preexisting meso-cracks. The test crack–meso-crack interactions also resulted in discontinuous crack growth. Discontinuities in crack extension, shown in Fig. 9(c), coincided with crack arrest at the meso-crack. Slow propagation continued while the meso-crack opened under the influence of the beam bending. The test crack then accelerated, and the process repeated itself whenever a new meso-crack was encountered. These interactions resulted in unusually large crack opening displacements, typically greater than 140 μm compared to 60–90 μm in all other systems. In contrast, crack propagation in Type I specimens was facilitated when the test crack linked with one of the parallel meso-cracks, as shown in Fig. 10(a). The change in the interaction between the test crack and these meso-cracks as the orientation of the test cracks was varied with specimen orientation among the three specimen types provided the fracture anisotropy.

The means by which toughening in Type III specimens is achieved, that is, crack deflection along the aggregate meso-cracks as speculated from surface images, can be fully confirmed using X-ray tomography. Fig. 11 presents tomographic cross-section taken through a fracture toughness specimen containing a test crack front that goes into the page. (From other tomographic measurements of as-processed samples, pre-existent meso-cracks of the order of 100–500 μm deep, and roughly the same size as the diameter of the non-textured island, were imaged. Microcracks, however, were not visible as their crack opening displacements are sub-micron, and below the resolution of this imaging technique.) It is apparent that the test crack has deflected 90° along the first aggregate

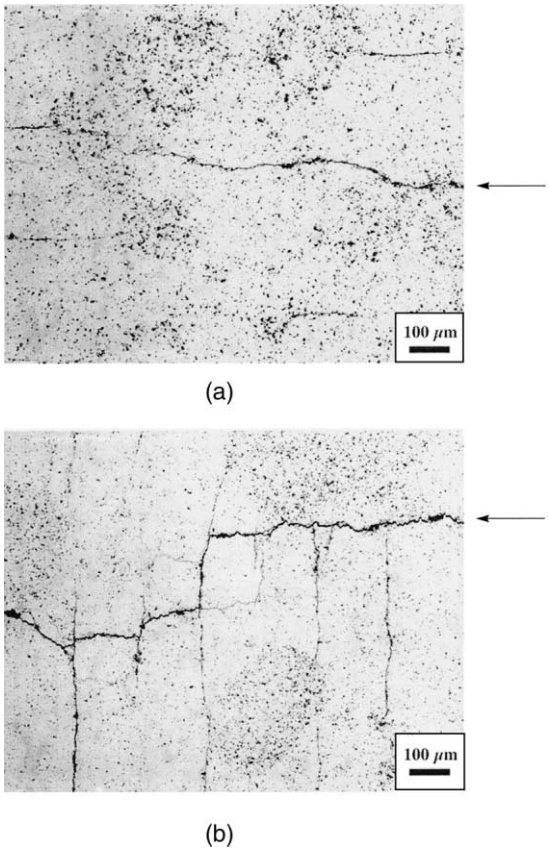

Fig. 10. Optical micrographs of typical crack paths for highly textured (a) Type I and (b) Type II specimens, showing interaction between the test crack and meso-cracks. Arrows indicate the test crack.

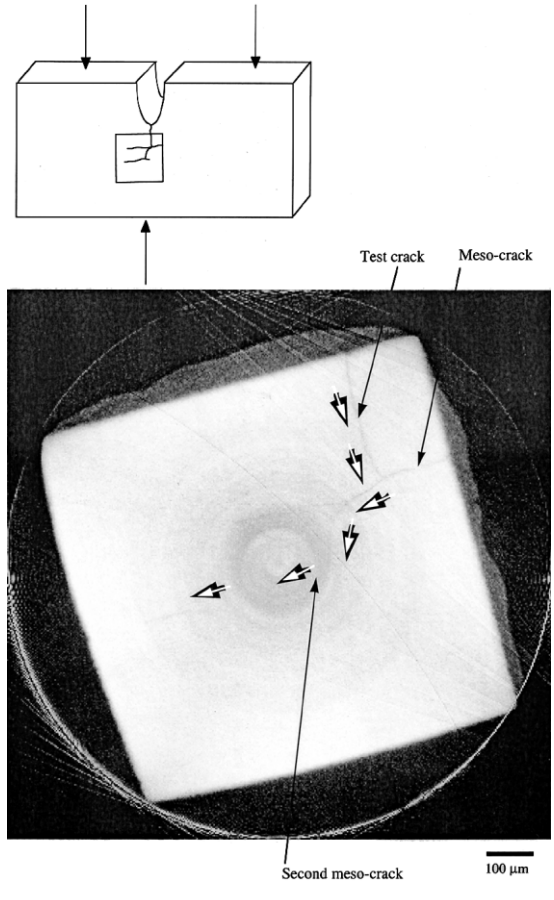

Fig. 11. X-ray tomograph of a fracture mechanics test specimen. The crack has deflected twice upon interaction with a series of meso-cracks deep within the material. Arrows indicate test crack trajectory.

crack, kinked out, grew parallel to the original direction of propagation, and then deflected 90° again into the second aggregate crack. These sections are proof that not only has micro-scale deflection occurred deep within this textured Fe_2TiO_5 specimen, but that the crack front is not planar. Furthermore, since the test crack grew under mixed mode conditions for at least some distance (which requires more energy than growing under pure mode I loading [43]) these crack patterns likely represent real increases in toughness. As a result, the tomography results are consistent with the enhanced toughness observed in any material that contained meso-cracks perpendicular to the crack plane. Moreover, they are a likely explanation of the decreased toughness in Type I specimens which had meso-cracks that ran parallel to the crack plane.

4. SUMMARY AND CONCLUDING REMARKS

By coupling the mechanical property results with residual stress measurements and simulations, small-angle neutron scattering measurements and X-ray tomography, it is possible to paint a complete picture of fracture in gelcast, textured iron titanate.

One of the most important changes in microstructure as a result of processing in a strong magnetic field was the introduction of a population of cracks having a very specific orientation. In all cases, these meso-cracks formed such that their planes were normal to the direction of the applied magnetic field during processing, which also corresponds to the *b*-axis texture axis. The cracks are related to residual stresses produced in the vicinity of non-textured 'aggregates' in a textured matrix. Their presence has been documented optically, by SANS, and by X-ray tomography.

X-ray residual stress measurements showed that significant stress relaxation had occurred during processing in all the specimens, regardless of the degree of crystallographic texture. The mechanisms of the relaxation are likely the formation of the meso-cracks and spontaneous microcracks. However, SANS results indicate that there is a small reduction in total crack surface area upon texturing indicative of a slight suppression of spontaneous microcracking. By simulating non-textured regions in a textured matrix, residual stresses consistent with the formation of cracks perpendicular to the applied magnetic field also are present. These simulations are consonant with SANS observations.

Highly anisotropic strength and R-curve behavior were observed in the textured materials. These measurements in combination with observations made during the course of the tests indicate that the measured anisotropies in mechanical behavior were primarily due to the presence of the meso-cracks. The strength dropped precipitously when the meso-cracks were oriented perpendicular to the long dimension of the beam. In other orientations, the strength remained near that of the control material.

Two trends are evident from toughness experiments. First, the degree of toughening increased with texture strength for all orientations. Second, the toughness was a strong function of the orientation of the fracture plane relative to the texture. This behavior was strongly influenced by the meso- and microcracks. The strongest interactions were observed in Type II configuration, in which the test crack propagated perpendicular to pre-existing meso-cracks, experiencing significant deflection. These interactions resulted in a peak fracture toughness approximately 2.5 times that of the control material.

It is interesting to note that the fracture properties in this study were improved by the formation of cracks coupled to texture, rather than the suppression of microcracking as was originally anticipated. This work suggests some strategies for toughening other single-phase, anisotropic materials in which texturing by any method might provide a means for inducing a series of cracks which serve as deflection sites. The texture associate cracking, however, implies an upper limit to which such properties may be improved by texturing. Should cracking be so prevalent in the bulk material that a connected network of cracks forms, a degradation in properties would be anticipated.

Acknowledgements—Funding for this work was provided by the National Science Foundation under Grant No. DMR-9800257. We are indebted to the late Professor Jerome B. Cohen for suggesting the tomography experiment and to Professor William Halperin of the Department of Physics and Astronomy, Northwestern University, whose magnet was used for these studies. Parts of this research were conducted at the National Synchrotron Light Source, Brookhaven National Laboratory, which is supported by the US Department of Energy, Division of Materials Sciences and Division of Chemical Sciences (DOE contract number DE-AC02-76CH00016). Thank you to John Dunsmuir for the excellent XMT beamline X2B at NSLS. We acknowledge the NIST Center for Neutron Research for the use of neutron beam facilities.

REFERENCES

1. Atzmony, U., Gurewitz, E., Melamud, M., Pinto, H., Shaked, H., Gorodetsky, G., Hermon, E., Hornreich, R. M., Shtrikman, S. and Wanklyn, B., *Phys. Rev. Lett.*, 1979, **43**, 782.
2. Atzmony, U., Gurewitz, E., Melamud, M., Pinto, H., Shaked, H., Gorodetsky, G., Hermon, E., Hornreich, R. M., Shtrikman, S. and Wanklyn, B., *J. Magn. Magn. Mater.*, 1980, **15–18**, 115.
3. Bayer, G., *J. Less-Common Met.*, 1971, **24**, 129.
4. Cleveland, J. J. and Bradt, R. C., *J. Am. Ceram. Soc.*, 1978, **61**, 478.
5. Buessam, W. R. and Lange, F. F., *Interceramics*, 1966, **15**, 229.
6. Davidge, R. W. and Tapin, G., *J. Mater. Sci.*, 1968, **3**, 297.
7. Siebeneck, H. J., Hasselman, D. P. H., Cleveland, J. J. and Bradt, R. C., *J. Am. Ceram. Soc.*, 1977, **60**, 336.
8. Rice, R. W. and Pohanka, R. C., *J. Am. Ceram. Soc.*, 1979, **62**, 559.
9. Case, E. D., Smyth, J. R. and Hunter, O. Jr., *J. Mater. Sci.*, 1981, **15**, 149.
10. Davidge, R., *Acta metall.*, 1981, **29**, 1695.
11. Claussen, N., Mussler, B. and Swain, M. V., *J. Am. Ceram. Soc.*, 1982, **65**, C14.

12. Fu, Y. and Evans, A. G., *Acta metall.*, 1985, **33**, 1525.
13. Thomas, H. A. J. and Stevens, R., *Br. Ceram. Trans. J.*, 1989, **88**, 184.
14. Paulik, S. W., Faber, K. T. and Fuller, E. R. Jr., *J. Amer. Ceram. Soc.*, 1994, **77**, 454.
15. Bradt, R. C., *Low Expansion Materials*, ed. D. P. Stinton and S. Y. Limaya, American Ceramic Society, Westerville, OH, 1995.
16. Paulik, S. W., Zimmerman, M. H., Faber, K. T. and Fuller, E. R. Jr., *J. Mater. Res.*, 1996, **11**, 2795.
17. Omatete, O. O., Janney, M. A. and Strehlow, R. A., *Am. Ceram. Soc. Bull.*, 1991, **70**, 1641.
18. Zimmerman, M. H., Faber, K. T. and Fuller, E. R. Jr., *J. Am. Ceram. Soc.*, 1997, **80**, 2725.
19. Pentecost, J. L. and Wright, C. H., *Advances in X-Ray Analysis*, Vol. 7, ed. W. M. Mueller, G. R. Mallett and M. Fay, Plenum Press, NY, 1964.
20. Russ, J. C., *Practical Stereology*. Plenum Press, New York, 1986.
21. Robinson, Q., Georgopoulos, P., Johnson, D. L., Marcy, H. O., Kannewurf, C. R., Hwu, S. -J., Marks, T. J., Poeppelmeier, K. R., Song, S. N. and Ketterson, J. B., *Adv. Ceram. Mater.*, 1987, **2**, 380.
22. Kostorz, G., in *Treatise in Materials Science and Technology*, Vol. 15. Academic Press, New York, 1979.
23. Kostorz, G., in *10th Discussion Conference on Small-Angle Scattering and Related Methods*. Hüthig and Wepf Verlag, Prague, 1987.
24. Porod, G., *Acta Phys. Astriaca*, 1949, **2**, 255.
25. Glinka, C. J., Rowe, J. M. and LaRock, J. G., *J. Appl. Cryst.*, 1985, **19**, 427.
26. Flannery, B. P., Deckman, H. W., Roberge, W. G. and D'Amico, K. L., *Science*, 1987, **237**, 1439.
27. Deckman, H. W., Dunsmuir, J. H., D'Amico, K. L., Ferguson, S. R. and Flannery, B. P., *Mater. Res. Soc. Proc.*, 1991, **217**, 97.
28. Langer, S., Carter, W. C., Fuller, E. R. Jr. and Roosen, A., *OOF*. National Institute of Standards and Technology, Gaithersburg, MD, 1997.
29. Matthies, S. and Vinel, G. W., *Phys. Stat. Sol. B*, 1982, **112**, K111.
30. Matthies, S., Wenk, H. R. and Vinel, G. W., *J. Appl. Crystallogr.*, 1988, **21**, 285.
31. Kallend, J. S., Kocks, U. F., Rollett, A. D. and Wenk, H. R., *Mater. Sci. Eng. A*, 1991, **132**, 1.
32. Zimmerman, M. H., Faber, K. T., Fuller, E. R. Jr., Kruger, K. L. and Bowman, K. J., *J. Am. Ceram. Soc.*, 1996, **79**, 1389.
33. Winholtz, R. A., *Peakfit: A Program to Fit Analytic Functions to Diffraction Peaks*, Northwestern University, 1988.
34. Winholtz, R. A. and Cohen, J. B., *Aust. J. Phys.*, 1988, **41**, 189.
35. Winholtz, R. A., *TRIAX: A Program to Calculate Triaxial Stresses and Associated Errors from Diffraction Data*, Northwestern University, 1989.
36. ASTM C1161-94, Standard Test Method for Flexural Strength of Advanced Ceramics at Ambient Temperature, *Annual Book of Standards*, Vol 15.01, ASTM, West Conshohocken, PA, 2000.
37. Kanninen, M. F., *Int. J. Fract.*, 1973, **9**, 83.
38. Forrest, M. M., *Engineer's Mini-Notebook*. Radio Shack, Fort Worth, 1994.
39. Tanaka, T., *Sci. Am.*, 1981, **244**, 124.
40. Russel, W. B., Saville, D. A. and Schowalter, W. R., *Colloidal Dispersions*. Cambridge University Press, Cambridge, 1989.
41. Allen, A. J., Fuller, Jr., E. R., Faber, K. T., Zimmerman, M. H. and J. S. Wallace, J. S., *Advanced Materials for the 21st Century: The 1999 Julia R. Weertman Symposium*, ed. Y.-W. Chung, D. C. Dunand, P. K. Liaw, and G. B. Olson, The Minerals, Metals & Materials Society, Warrendale, PA, 1999.
42. Tewary, V. K. and Fuller, E. R. Jr., *J. Mater. Res.*, 1990, **5**, 1118.
43. Faber, K. T. and Evans, A. G., *Acta metall.*, 1982, **31**, 565.